IEEE Access
Multidisciplinary | Rapid Review | Open Access Journal

Received May 16, 2018, accepted June 14, 2018, date of publication June 22, 2018, date of current version July 25, 2018.

Digital Object Identifier 10.1109/ACCESS.2018.2849857

Accurate Prediction and Analysis of Electromagnetic Fields and Forces in Flux-Focusing Eddy Current Coupling With Double Slotted Conductor Rotors

ZHAO LI, DAZHI WANG, AND DI ZHENG
School of Information Science and Engineering, Northeastern University, Shenyang 110819, China
Corresponding author: Dazhi Wang (lz.b.y@163.com)

This work was supported in part by the National Key R&D program of China under Grant 2017YBF1300900 and in part by the Fundamental Research Funds for the Central Universities under Grant N160406001.

ABSTRACT Permanent magnet eddy current couplings are promising devices for torque and speed transmission without any mechanical contact. In this paper, flux-focusing permanent magnet eddy current couplings with double slotted conductor rotors are proposed and investigated. Given the drawback of the accurate 3-D finite element method, the purpose of this paper lies to establish an accurate and fast analytical model to evaluate the electromagnetic field and torque of such devices with non-homogeneous boundary conditions. Thus, based on the 2-D sub-domain method, the magnetic vector potential in each sub-domain is formulated and solved by the separation of variables method. Taking into account the eddy current effects and slotting effects, the closed-form expressions of magnetic field, induced current, electromagnetic force, and torque for such devices are obtained. Finally, the 3-D finite element method is employed to validate the analytical results.

INDEX TERMS Permanent magnet, coupling, electromagnetic fields, sub-domain model.

I. NOMENCLATURE

l_1	Inner radius of PM rotor.
l_2	Outer radius of PM rotor.
h	Over length of conductor rotor.
a	Thickness of conductor disk ($a = e - d$).
$b - a$	Air-gap length ($b - a = d - c$).
$c - b$	Thickness of PM.
p	Number of pole-pairs.
q	Numbers of conductor slots.
σ	Conductivity of conductor disk.
θ_i	The initial angular position of the ith PM.
α_i	The initial angular position of the ith conductor spoke.
β	Opening angle of PM
β_1	Angle of each conductor spoke
$N(n)$	Number of spatial harmonics in PM region
$K(k)$	Number of spatial harmonics in conductor region
$G(g)$	Number of spatial harmonics in air-gap region
$M(m)$	Number of time harmonic

II. INTRODUCTION

Eddy current couplings based on permanent magnets (PMs) are developed to transmit power and adjust speed between two shafts without any mechanical friction. The torque is transmitted from the prime mover to the output shaft through the magnetic field interaction in the air-gap. Relative to conventional mechanical couplings and adjustment devices, such contactless devices can provide many advantages, like lower sensitivity to shaft misalignment and vibration, greater tolerance to harsh environments and severe case, and more energy-efficient (low slip region) [1]–[3]. Therefore, they are welcome in diverse industries, such as transmission, brake, damping, and isolated systems [4]–[6].

Regarding the rotational permanent magnet eddy current couplings, there are mainly two types: axial and radial flux topology, which are also known as disk and concentric topology. Considering the position of the PMs in the back iron, these devices may likewise be grouped into two categories: surface mounting and interior embedded PM configuration. In recent years, academe's study puts too much emphasis

on the former, however, few studies have been undertaken about the latter. Based on an extensive investigation on interior embedded PM devices [7]–[9], it can be discovered that such structure presents some remarkable advantages, such as robust rotor construction and high irreversible demagnetization withstand, which will increase the lifespan of the working devices. But for flux-focusing (interior embedded PM) eddy current couplings, one of the main drawback is that the output torque is decreased when they are compared with the surface mounting couplings with the same specifications [8]. To overcome this problem, some improvements to the structure have to be done. In our previous study [10], double-sided conductor rotor is applied to improve the torque density with the increase of volume and weight. In [11] and [12], another method is proposed to improve the torque density, where the eddy current path is guided by slotting the conductor rotor. They bring us a good idea to develop the flux-focusing eddy current couplings with double slotted conductor rotors, as shown in Fig. 1.

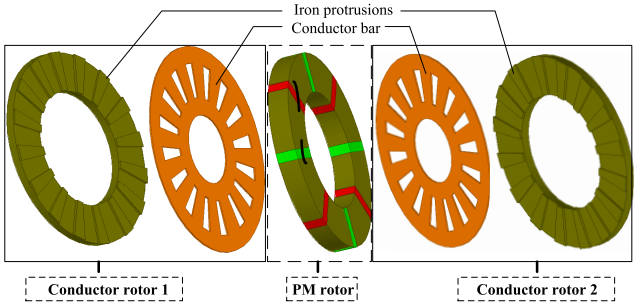

FIGURE 1. Exploded view of flux-focusing eddy current coupling with double slotted conductor rotors.

To analyze the key performances of such devices, for example, torque-slip speed characteristic, it is necessary to know the accurate magnetic field distribution. So far, the most commonly used methods to evaluate the electromagnetic fields are numerical approaches [13]–[15], and the analytical approaches [1]–[3], [16]–[18]. With numerical approaches, like finite element analysis (FEA), the accurate analysis results can be obtained by considering the real geometrical structure and nonlinear physical properties of materials. However, they will require huge memory and take a lot of time, especially by the 3-D FEA. By contrast, analytical approaches, based on the simplifying assumptions, can obtain satisfactory results quickly and explicitly. Therefore, analytical approaches are introduced as an ideal alternative to the numerical approaches in the early design stage of electromagnetic devices.

Among the analytical approaches, the 2-D layer method is widely used to predict the magnetic field in the traditional surface-mounted PM eddy current couplings. The solution is usually performed on the basis of field equations by the variable separation method (VSM). Moreover, to reduce the 3-D problem to a 2-D one, the geometrical structure is linearly treated. More recently [19], [20], the 3-D analytical model for axial-flux eddy current couplings has been presented. However, the two methods mentioned are not suitable for the proposed topology in this paper, because there are pretty sophisticated boundary conditions in the PM rotor and conductor rotor domain, where the inhomogeneous material properties exist. In addition, magnetic equivalent circuit (MEC) is another simple analytical approach, which has been employed to evaluate the performances of various PM eddy current couplings [8], [21]. The drawback of this approach is that we have to determine the magnetic network (or circuit) and the corresponding reluctance in advance, which will increase its complexity and unreliability.

To solve such rotating electromagnetic field problem with complex boundary conditions, sub-domain model can be employed, which has been widely used in PM devices with slotting effects. Similarly to the 2-D layer analytical method, the sub-domain model divides the whole domain into different sub-domains, such as air-gap, magnets, iron cores, and slots. The field distribution in each sub-domain is directly obtained by solving the governing equations based on the classical interface conditions. Using this approach, analytical models for the eddy current loss of PM synchronous machines with surface-inset PMs [22], the magnetic field distribution of axial-field magnetic gears [23], the electromagnetic torque of surface-inset PM motors [24], and surface-mounted PM eddy current couplers with slotted conductor [12] have been presented. But their topologies are different from the proposed flux-focusing eddy current coupling with double slotted conductor rotors, whose PM rotor and conductor rotor can be viewed as slotted topology during modeling.

III. DEVICES GEOMETRY AND ASSUMPTIONS

A. GEOMETRY

A schematic of the studied eddy current coupling is shown in Fig. 1. As described in Fig. 1, the device consists of two parts: PM rotor and two conductor rotors (mostly copper). Different from conventional structure [1], [3], [18]–[21], the magnets inserted into the iron cores are circumferentially magnetized, and the conductor plates are slotted and filled with protrusions of back iron. It should be noted that such devices can also be applied in speed regulation system, where a screw mechanism is equipped to adjust the length of air gap. Fig. 2 shows the geometry of the investigated eddy current coupling. The corresponding parameters are as follows

1) The inner and outer radii of the PMs are l_1 and l_2, respectively;
2) The thickness of the PMs is $c - b$;
3) The length of the air gap is $b - a$;
4) The thickness of slotting conductor disk is a;
5) The numbers of pole-pairs and conductor slots are p and q, respectively;
6) The initial angular position of the ith PM is θ_i, and can be defined by

$$\theta_i = -\beta/2 + i\pi/2 + \beta_0 \quad \text{with} \quad i = 1, 2, \cdots, 2p \qquad (1)$$

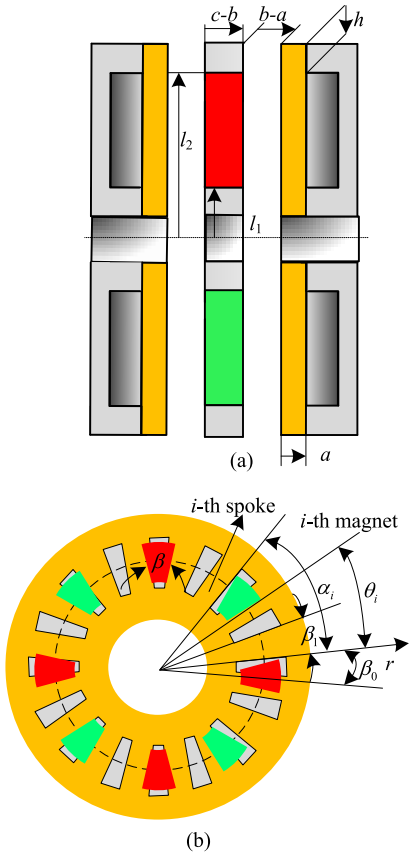

FIGURE 2. Geometry of the study subject. (a) Geometric parameters and (b) exploded view along the axial direction.

where, β is the PM opening angle; β_0 is the offset angel of z-axial in a frame system.

7) The initial angular position of the ith conductor spoke is α_i, and can be defined by

$$\alpha_i = 2\pi\,(i-1)\,/q \quad \text{with} \quad i = 1, 2, \cdots, q \tag{2}$$

It is quite obvious that 2) can be achieved by setting the value of β_0. Herein, to simplify the analysis, the value of β_0 is set to zero.

8) The angle of each conductor spoke is $\beta_1 = 2\pi\beta_2/q$, where β_2 is the ratio between spoke arc and slot pitch.

B. MODELING ASSUMPTIONS

Due to the special rotor structure, it will be very difficult to establish the 3-D analytical field model of such devices. A more general approach is to convert the 3-D problem into a 2-D problem. More importantly, the above simplification doesn't seriously affect the reliability and adaptability of analytical model [1], [17], [18]. This implies that the edges effects can be neglected. Inspired by the approach above, in this paper, a simplified 2-D analytical model is obtained, as shown in Fig. 3. In practice, the structure is imagined to unfold along the circumferential direction at the average

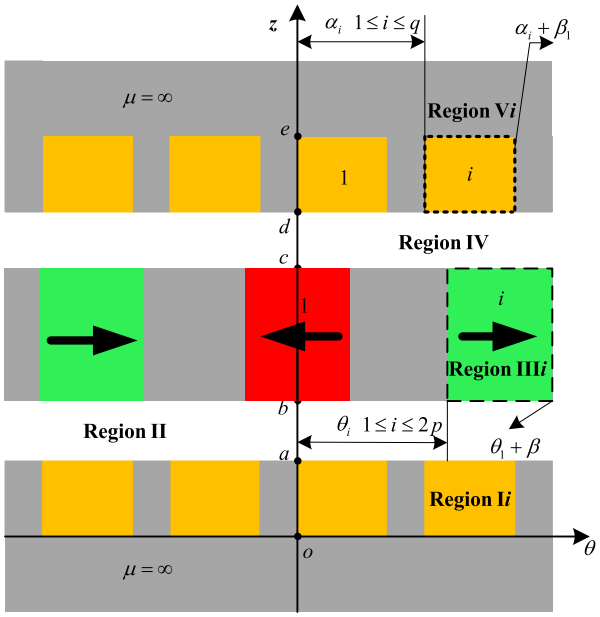

FIGURE 3. 2-D analytical model.

radius ($R_{av} = (l_1 + l_2)/2$). A 2-D cylindrical coordinates is used to describe the system problem, where θ-axial denotes the tangential direction, z-axial denotes the axial direction. Moreover, θ component and z component don't depend on the radial (r-direction) component.

To simplify the analytical modeling, some reasonable assumptions, commonly employed in the modeling of such devices, are adopted as follows

1) Iron core and back iron have infinite permeability, and there are no induced currents generated in these regions.
2) The magnetic vector potential in every layer has only r-direction component and only depends on z and θ.
3) The magnet has linear properties.
4) The permeability of the conductor plate, the PMs, and the air is μ_0.
5) The eddy current density is distributed uniformly in the conductor spoke, and only has the r-direction component.
6) All the interfaces are defined as the constant.

As shown in Fig. 3, based on the above-mentioned assumptions, the whole 2-D model is divided into five sub-domains, namely, the ith PM sub-domain (region **III*i***), the air-gap sub-domain (region **II** and **IV**), and the ith conductor spoke sub-domain (region **I*i*** and**V*i***). According to the relationship between the magnetic vector potential and the flux density, the system problem is converted into the solution of magnetic vector potential in each sub-domain.

In order to easily solve the eddy current generated in conductor spoke region, the moving permanent magnet is treated as the traveling wave magnetic field source [12], [18], [25], then all the field quantities depend on the time variable t, some notations are used in this paper as follows

1) The ith conductor spoke sub-domain

$$\mathbf{A}_i^{\mathbf{I}} = A_i^I(\theta, z, t)\overrightarrow{e_r} = \Re[\tilde{A}_i^I(\theta, z)e^{j\lambda_0 t}]\overrightarrow{e_r}$$
$$\mathbf{A}_i^{\mathbf{V}} = A_i^V(\theta, z, t)\overrightarrow{e_r} = \Re[\tilde{A}_i^V(\theta, z)e^{j\lambda_0 t}]\overrightarrow{e_r}$$

2) Air-gap sub-domain

$$\mathbf{A}^{\mathbf{II}} = A^{II}(\theta, z, t)\overrightarrow{e_r} = \Re[\tilde{A}^{II}(\theta, z)e^{j\lambda_0 t}]\overrightarrow{e_r}$$
$$\mathbf{A}^{\mathbf{IV}} = A^{IV}(\theta, z, t)\overrightarrow{e_r} = \Re\,[\tilde{A}^{IV}(\theta, z)e^{j\lambda_0 t}]\overrightarrow{e_r}$$

3) The ith PM sub-domain

$$\mathbf{A}_i^{\mathbf{III}} = A_i^{III}(\theta, z, t)\overrightarrow{e_r} = \Re[\tilde{A}_i^{III}(\theta, z)e^{j\lambda_0 t}]\overrightarrow{e_r}$$

where, a tilde over a variable denotes its complex form and $j = \sqrt{-1}$, $\Re$ denotes the real part, $\overrightarrow{e_r}$ is the unit vector in the r-direction, λ_0 is the angular frequency and can be expressed as

$$\lambda_0 = 2\pi n_1 mps/60 \tag{3}$$

where, m is the mth time harmonic, n_1 is the input speed, and s is the slip. However, to facilitate the expressions, the time harmonic is not given in the solution of $\mathbf{A}$ in every domain.

IV. MAGNETIC VECTOR POTENTIAL CALCULATION

Owning to the inconsistent material properties in sub-domain III, and the slotting effects in sub-domain I and V, discontinuous boundary condition problems have occurred at the interfaces between sub-domain I and II, II and III, III and IV, IV and V; thus, the conventional layer model theory is infeasible. Herein, the accurate sub-domain model approach is employed to solve the complex electromagnetic field problem by taking into account the effects of the eddy currents on the magnetic flux density distribution and the time-space harmonics.

To simplify the analytical expressions, some notations are adopted as follows

$$\lambda_k = \frac{k\pi}{\beta R_{av}}, \quad \lambda_n = \frac{n}{R_{av}}, \quad \lambda_g = \frac{g\pi}{\beta_1 R_{av}} \tag{4}$$

A. PM SUB-DOMAIN (REGION III)

In the ith PM sub-domain, the problem to solve is the Poisson equation as follows

$$\nabla^2 A_i^{III} = -\mu_0 \nabla \times \overrightarrow{M_i} \quad \text{for} \begin{cases} b \le z \le c \\ \theta_i \le \theta \le \theta_i + \beta. \end{cases} \tag{5}$$

with

$$\overrightarrow{M_i} = (-1)^i \frac{B_r}{\mu_0}\overrightarrow{e_\theta} \tag{6}$$

where, B_r is the residual magnetization; $\overrightarrow{e_\theta}$ is the unit vector in the θ-direction.

Because of the PMs being tangentially magnetized with the fixed residual magnetization, (5) can be simplified to a Laplace equation, of which differential form can be expressed by

$$\frac{1}{R_{av}^2}\frac{\partial^2 A_i^{III}}{\partial\theta^2} + \frac{\partial^2 A_i^{III}}{\partial z^2} = 0 \quad \text{for} \begin{cases} b \le z \le c \\ \theta_i \le \theta \le \theta_i + \beta \end{cases} \tag{7}$$

Considering the flux lines are normal to the interfaces $\theta = \theta_i$ and $\theta = \theta_i + \beta$, the boundary conditions are defined as follows

$$\left.\frac{\partial A_i^{III}}{\partial\theta}\right|_{\theta=\theta_i} = 0, \quad \left.\frac{\partial A_i^{III}}{\partial\theta}\right|_{\theta=\theta_i+\beta} = 0 \tag{8}$$

According to the continuity of the magnetic vector potential between the ith PM sub-domain and region II and IV, more boundary conditions are given by

$$A_i^{III}(\theta, b) = A^{II}(\theta, b) \tag{9}$$
$$A_i^{III}(\theta, c) = A^{IV}(\theta, c) \tag{10}$$

Considering the boundary condition (8), by using the variable separation method, the general solution of (7) can be given by [10], [16]

$$\begin{aligned} A_i^{III}(\theta, z) &= a_0^{IIIi} + b_0^{IIIi} z \\ &\quad + \sum_{k=1}^{\infty}\left(\frac{a_k^{IIIi}\mathrm{sh}[\lambda_k(z-c)]}{\mathrm{sh}[\lambda_k(b-c)]} + \frac{b_k^{IIIi}\mathrm{sh}[\lambda_k(z-b)]}{\mathrm{sh}[\lambda_k(c-b)]}\right) \\ &\quad \times\cos[\lambda_k R_{av}(\theta-\theta_i)] \end{aligned} \tag{11}$$

where, k is the order of the spatial harmonics in this region. The unknown constant coefficients a_0^{IIi}, b_0^{IIi}, a_k^{IIi}, and b_k^{IIi} are determined using the Fourier series expansion method with the interface conditions (9) and (10) over the interval $[\theta_i, \theta_i + \beta]$, and can be expressed by [23], [24], [29]

$$a_0^{IIIi} + b_0^{IIIi} z\Big|_{z=b} = \frac{1}{\beta}\int_{\theta_i}^{\theta_i+\beta} A^{II}(\theta, b)d\theta \tag{12}$$

$$a_0^{IIIi} z + b_0^{IIIi}\Big|_{z=c} = \frac{1}{\beta}\int_{\theta_i}^{\theta_i+\beta} A^{IV}(\theta, c)d\theta \tag{13}$$

$$a_k^{IIIi} = \frac{2}{\beta}\int_{\theta_i}^{\theta_i+\beta} A^{II}(\theta, b)\cos[\lambda_k R_{av}(\theta-\theta_i)]d\theta \tag{14}$$

$$b_k^{IIIi} = \frac{2}{\beta}\int_{\theta_i}^{\theta_i+\beta} A^{IV}(\theta, c)\cos[\lambda_k R_{av}(\theta-\theta_i)]d\theta \tag{15}$$

B. AIR-GAP SUB-DOMAIN (REGION II and IV)

In the air-gap region, Laplace equation can be written as follows

$$\frac{1}{R_{av}^2}\frac{\partial^2 A^{II}}{\partial\theta^2} + \frac{\partial^2 A^{II}}{\partial z^2} = 0 \quad \text{for} \begin{cases} a \le z \le b \\ 0 \le \theta \le 2\pi. \end{cases} \tag{16}$$

Different from the surface-mounted model and slotless model, the boundary conditions for such devices are complicated for the discontinuity. According to the continuity of the tangential magnetic field at the interface $z = b$, one boundary condition can be written as

$$\left.\frac{\partial A^{II}}{\partial z}\right|_{z=b} = f_1(\theta) \tag{17}$$

with

$$f_1(\theta) = \begin{cases} \left.\dfrac{\partial A_i^{III}}{\partial z}\right|_{z=b} + (-1)^i B_r, \forall\theta \in [\theta_i, \quad \theta_i + \beta] \\ 0, \qquad\qquad\qquad\qquad\qquad\qquad else \end{cases} \tag{18}$$

For the same reason, another boundary condition at the interface $z = a$ can be expressed by

$$\left.\frac{\partial A^{II}}{\partial z}\right|_{z=a} = f_2(\theta) \tag{19}$$

with

$$f_2(\theta) = \begin{cases} \left.\dfrac{\partial A_i^{I}}{\partial z}\right|_{z=a}, \quad \forall\theta \in [\alpha_i, \alpha_i + \beta_1] \\ 0, \qquad\qquad\qquad else \end{cases} \tag{20}$$

By using the variable separation method, the analytic series can be given by [24]

$$A^{II}(\theta, z) = a_0^{II} + \sum_{n=1}^{\infty} \frac{1}{\lambda_n} \left(\begin{matrix} a_n^{II} \dfrac{\mathrm{ch}[\lambda_n (z-a)]}{\mathrm{sh}[\lambda_n (b-a)]} \\ + b_n^{II} \dfrac{\mathrm{ch}[\lambda_n (z-b)]}{\mathrm{sh}[\lambda_n (a-b)]} \end{matrix} \right) \cos(n\theta) + \sum_{n=1}^{\infty} \frac{1}{\lambda_n} \left(\begin{matrix} c_n^{II} \dfrac{\mathrm{ch}[\lambda_n (z-a)]}{\mathrm{sh}[\lambda_n (b-a)]} \\ + d_n^{II} \dfrac{\mathrm{ch}[\lambda_n (z-b)]}{\mathrm{sh}[\lambda_n (a-b)]} \end{matrix} \right) \sin(n\theta) \tag{21}$$

where, n is the order of the spatial harmonics in this region. The unknown constant coefficients a_n^{III}, b_n^{III}, c_n^{III} and d_n^{III} are determined using the Fourier series expansion method with the interface conditions (17) and (19), respectively, and can be expressed as

$$a_n^{II} = \frac{1}{\pi} \sum_{i=1}^{2p} \int_{\theta_i}^{\theta_i+\beta} \left[\left.\frac{\partial A_i^{III}}{\partial z}\right|_{z=b} + (-1)^i B_r \right] \cos(n\theta) d\theta \tag{22}$$

$$b_n^{II} = \frac{1}{\pi} \sum_{i=1}^{q} \int_{\alpha_i}^{\alpha_i+\beta_1} \left.\frac{\partial A_i^{I}}{\partial z}\right|_{z=a} \cos(n\theta) d\theta \tag{23}$$

$$c_n^{II} = \frac{1}{\pi} \sum_{i=1}^{2p} \int_{\theta_i}^{\theta_i+\beta} \left[\left.\frac{\partial A_i^{III}}{\partial z}\right|_{z=b} + (-1)^i B_r \right] \sin(n\theta) d\theta \tag{24}$$

$$d_n^{II} = \frac{1}{\pi} \sum_{i=1}^{q} \int_{\alpha_i}^{\alpha_i+\beta_1} \left.\frac{\partial A_i^{I}}{\partial z}\right|_{z=a} \sin(n\theta) d\theta \tag{25}$$

For the same reason, the magnetic vector potential in region IV can be expressed by

$$A^{IV}(\theta, z) = a_0^{IV} + \sum_{n=1}^{\infty} \frac{1}{\lambda_n} \left(\begin{matrix} a_n^{IV} \dfrac{\mathrm{ch}[\lambda_n (z-d)]}{\mathrm{sh}[\lambda_n (c-d)]} \\ + b_n^{IV} \dfrac{\mathrm{ch}[\lambda_n (z-c)]}{\mathrm{sh}[\lambda_n (d-c)]} \end{matrix} \right) \cos(n\theta) + \sum_{n=1}^{\infty} \frac{1}{\lambda_n} \left(\begin{matrix} c_n^{IV} \dfrac{\mathrm{ch}[\lambda_n (z-d)]}{\mathrm{sh}[\lambda_n (c-d)]} \\ + d_n^{IV} \dfrac{\mathrm{ch}[\lambda_n (z-c)]}{\mathrm{sh}[\lambda_n (d-c)]} \end{matrix} \right) \sin(n\theta) \tag{26}$$

where,

$$a_n^{IV} = \frac{1}{\pi} \sum_{i=1}^{2p} \int_{\theta_i}^{\theta_i+\beta} \left[\left.\frac{\partial A_i^{III}}{\partial z}\right|_{z=c} + (-1)^i B_r \right] \cos(n\theta) d\theta \tag{27}$$

$$b_n^{IV} = \frac{1}{\pi} \sum_{i=1}^{q} \int_{\alpha_i}^{\alpha_i+\beta_1} \left.\frac{\partial A_i^{V}}{\partial z}\right|_{z=d} \cos(n\theta) d\theta \tag{28}$$

$$c_n^{IV} = \frac{1}{\pi} \sum_{i=1}^{2p} \int_{\theta_i}^{\theta_i+\beta} \left[\left.\frac{\partial A_i^{III}}{\partial z}\right|_{z=c} + (-1)^i B_r \right] \sin(n\theta) d\theta \tag{29}$$

$$d_n^{IV} = \frac{1}{\pi} \sum_{i=1}^{q} \int_{\alpha_i}^{\alpha_i+\beta_1} \left.\frac{\partial A_i^{V}}{\partial z}\right|_{z=d} \sin(n\theta) d\theta \tag{30}$$

C. CONDUCTOR SUB-DOMAIN (REGION I and V)

In the ith conductor spoke sub-domain, because of the appearance of the induced currents, the field equation in region V is written as follows

$$\nabla^2 A_i^V = -\mu_0 J_i^V \quad \text{for} \quad \begin{cases} d \le z \le e \\ \alpha_i \le \theta \le \alpha_i + \beta_1. \end{cases} \tag{31}$$

where, the induced current in the ith conductor spoke, based on Faraday law, can be expressed as

$$J_i^V = -\sigma \frac{\partial A_i^V}{\partial t} = -j\sigma mp\omega_s A_i^V \tag{32}$$

where, $\omega_s = 2\pi n_1 s/60$. Accordingly, the filed equation (31) is further written as

$$\frac{1}{R_{av}^2} \frac{\partial^2 A_i^V}{\partial \theta^2} + \frac{\partial^2 A_i^V}{\partial z^2} = -j\mu_0 \sigma mp\omega_s A_i^{IV} \tag{33}$$

According to the flux lines are normal to the interfaces $\theta = \alpha_i$ and $\theta = \alpha_i + \beta_1$, and the continuity of the tangential magnetic field at the interface $z = d$, a group of boundary conditions are given by

$$\left.\frac{\partial A_i^{IV}}{\partial \theta}\right|_{\theta=\alpha_i} = 0, \quad \left.\frac{\partial A_i^{IV}}{\partial \theta}\right|_{\theta=\alpha_i+\beta_1} = 0, \quad \left.\frac{\partial A_i^{IV}}{\partial z}\right|_{z=e} = 0 \tag{34}$$

In addition, the other one is the continuity of the magnetic vector potential between region IV and III at the interface $z = d$, which is expressed as

$$A_i^V(\theta, d) = A^{IV}(\theta, d) \tag{35}$$

During the solutions, the complicated field equation (33) is transformed into a Sturm–Liouville problem by employing the variable separation method. Taking into account the interface condition (34), the solution of (33) is derived by [12]

$$A_i^V(\theta, z) = a_0^{Vi} \frac{\mathrm{ch}[\Lambda_1 (z-e)]}{\mathrm{ch}[\Lambda_1 (d-e)]} + \sum_{g=1}^{\infty} a_g^{Vi} \frac{\mathrm{ch}[\Lambda_2 (z-e)]}{\mathrm{ch}[\Lambda_2 (d-e)]} \times \cos[\lambda_g R_{av} (\theta - \alpha_i)] \tag{36}$$

where,

$$\Lambda_1 = \sqrt{j\mu_0 \sigma mp\omega_s} \tag{37}$$

$$\Lambda_2 = \sqrt{\lambda_g^2 + \Lambda_1^2} \tag{38}$$

where, g is the order of the spatial harmonics in this region. The unknown constant coefficients a_0^{Vi} and a_g^{Vi} are determined using the Fourier series expansion method with the interface condition (35) over the interval $[\alpha_i, \alpha_i + \beta_1]$, and can be expressed by

$$a_0^{Vi} = \frac{1}{\beta_1}\int_{\alpha_i}^{\alpha_i+\beta_1} A^{IV}(\theta, d)d\theta \tag{39}$$

$$a_g^{Vi} = \frac{2}{\beta_1}\int_{\alpha_i}^{\alpha_i+\beta_1} A^{IV}(\theta, d)\cos[\lambda_g R_{av}(\theta-\alpha_i)]d\theta \tag{40}$$

For the same reason, the magnetic vector potential in region I can be expressed by

$$A_i^I(\theta, z) = a_0^{Ii}\frac{\mathrm{ch}(\Lambda_1 z)}{\mathrm{ch}(\Lambda_1 a)} + \sum_{g=1}^{\infty} a_g^{Ii}\frac{\mathrm{ch}(\Lambda_2 z)}{\mathrm{ch}(\Lambda_2 a)}\cos[\lambda_g R_{av}(\theta-\alpha_i)] \tag{41}$$

where,

$$a_0^{Ii} = \frac{1}{\beta_1}\int_{\alpha_i}^{\alpha_i+\beta_1} A^{II}(\theta, a)d\theta \tag{42}$$

$$a_g^{Ii} = \frac{2}{\beta_1}\int_{\alpha_i}^{\alpha_i+\beta_1} A^{II}(\theta, a)\cos[\lambda_g R_{av}(\theta-\alpha_i)]d\theta \tag{43}$$

As indicated in [23], the Laplace equation (16) with the Neumann boundary conditions (17) and (19) should satisfy the following condition,

$$\int_0^{2\pi}\left(\frac{\partial A^{II}}{\partial z}\bigg|_{z=a} - \frac{\partial A^{II}}{\partial z}\bigg|_{z=b}\right)d\theta = 0 \tag{44}$$

Substituting (11) and (41) into (44), the further procession provides an important constraint condition by

$$\sum_{i=1}^{q} a_0^{Ii}\Lambda_1\tanh(\Lambda_1 a)\beta_1 = \sum_{i=1}^{2p} b_0^{IIIi}\beta \tag{45}$$

A point worth emphasizing is that, based on the working principle of such devices, the sum of the total induced currents produced in the conductor spokes is zero [12], [29], which is given by

$$\sum_{i=1}^{q}[J_i^V(t, m) + J_i^I(t, m)] = 2\sum_{i=1}^{q} J_i^V(t, m) = 0 \tag{46}$$

where, $J_i^V(t, m)$ denotes the mth time harmonic component of the induced currents flowing in the ith conductor spoke. According to (11), it is simplified as

$$\sum_{i=1}^{q} a_0^{Vi} = 0, \quad \sum_{i=1}^{q} a_0^{Ii} = 0 \tag{47}$$

In fact, (47) suggests that the induced currents in each spoke are not independent, but interacting with each other. Moreover, a_0^{IVi} greatly impacts the analytical predictions of magnetic field and eddy currents. To substitute (47) into (44), another constraint condition for (11) is obtained by

$$\sum_{i=1}^{2p} a_0^{IIIi} = 0 \tag{48}$$

D. EXPRESSION FORM OF SYSTEM EQUATIONS

Considering the complexity of the solutions for the integration constants, some professional mathematical tools, for example, MATLAB, is likely to be required. Therefore it is necessary to establish the matrix expression form of system equations. Assuming that N represents the number of spatial harmonics used in region **II** and **IV**; K represents the number of spatial harmonics used in region **I*i*** and **V*i***, and G represents the number of spatial harmonics used in region **III*i***. To substitute the expression for the magnetic vector potential in every subdomain into the solutions of the integration constants, the linear system equations can be formed and described in the matrix form as

$$\mathbf{MX} = \mathbf{Y} \tag{49}$$

where, **M**, **X**, and **Y** are the constant coefficient matrix, and the undetermined variable vector, and a constant source vector, respectively. Their detailed expressions are given in the Appendix.

E. FLUX DENSITY DISTRIBUTION

According to the definition of the magnetic vector potential, the tangential and axial components of the magnetic flux density in air-gap regions are deduced by

$$\begin{cases} B_\theta^{II,IV} = \dfrac{\partial A^{II,IV}}{\partial z} \\ B_z^{II,IV} = -\dfrac{1}{R_{av}}\dfrac{\partial A^{II,IV}}{\partial \theta} \end{cases} \tag{50}$$

As mentioned above, these results don't not reflect the time harmonics. Therefore, in the application process, the results are the superposition of different time harmonics.

F. AXIAL FORCE AND TORQUE

Axial-flux couplings have large axial force, which affects the rotor structure and bearing lifetime. For the studied eddy current coupling, there is the maximal attraction force while the slip speed is null. Therefore, axial magnetic force is an important parameter for an axial-flux eddy current coupling. In consideration of the complete symmetry of such devices, using the Maxwell stress tensor, the axial force is obtained by [19], [24]

$$F = \frac{2}{4\mu_0}\int_{l_1}^{l_2}\int_0^{2\pi}\left[\left|B_z^{II}\right|^2 - \left|B_\theta^{II}\right|^2\right]d\theta dr \tag{51}$$

The output torque of such devices consists of two types of torque, namely, electromagnetic torque and cogging torque. The electromagnetic torque, excluding the cogging torque, can be evaluated by using the eddy-current loss in the conductor spokes [1], [3], [8], [10]. Thus, such torque can be derived by [10]

$$T_e = \frac{P}{\omega_s} \tag{52}$$

with

$$P = \frac{l_1 - l_2}{\sigma_0} \sum_{i=1}^{q} \int_{\alpha_i}^{\alpha_i+\beta_1} \int_{d}^{e} \left| J_i^V \right|^2 dz d\theta \tag{53}$$

Studies have shown that the predicted results from (52) have some deviations from the real values. The main reason is that the tangential component of eddy current distributed in the overhang and central regions, according to the modeling assumption, is neglected. To overcome this problem, the Russell–Norsworthy (R–N) correction factor has been widely used and achieved good results, but only for the lower slip case [1], [12], [25], which can be expressed by

$$k_r = 1 - \frac{\tanh[\frac{\pi(l_2-l_1)}{\tau}]}{\frac{\pi(l_2-l_1)}{\tau}\left(1 + \tanh[\frac{\pi(l_1-l_2)}{\tau}] \cdot \tanh(\frac{\pi h}{\tau})\right)} \tag{54}$$

where, τ is the pole pitch.

When working at the high slip case, the eddy current distribution pattern has changed, thus the premise of R–N correction factor is no longer satisfied. A modified correction factor, which can be applied at any slip case, is introduced as follows [18]

$$k_r' = \begin{cases} k_r, & S \in [0, s_l) \\ \dfrac{[(1-k_r)s + (k_r S_h - S_l)]}{S_h - S_l}, & S \in [S_l, S_h] \\ 1, & S \in (S_h, 1]. \end{cases} \tag{55}$$

with

$$\begin{cases} s_l = \gamma_1 s_c \\ s_h = (k_r)^{\gamma_2} s_c \end{cases} \tag{56}$$

where, $\gamma_1 = 0.3$ and $\gamma_2 = -0.8$ are empirical factors [18]; s_c is the critical slip and derived by [25]

$$s_c = \frac{60}{p\mu_0\sigma a \tau n_1}\sqrt{\frac{b}{\Lambda_7 \Lambda_8}} \tag{57}$$

where,

$$\Lambda_7 = \frac{1}{2}[1 - \frac{\pi^2}{24}(\frac{\Lambda_8}{l_2 - l_1 + 2h})^2] \tag{58}$$

$$\Lambda_8 = 2\left[\frac{(l_2 - l_1)h_1}{\pi}\right]^{0.5} \tag{59}$$

Therefore, the corrected electromagnetic torque is further expressed as

$$T_{r-e} = k_r' T_e \tag{60}$$

According to [23], using the Maxwell stress tensor, the cogging torque can be computed by

$$T_{cogg} = \frac{R_m(l_2 - l_1)}{2\mu_0} \int_0^{2\pi} B_\theta^{III} B_z^{III} d\theta \tag{61}$$

The total output torque of such devices can be expressed as

$$T_o = 2(T_{r-e} + T_{cogg}) \tag{62}$$

V. VALIDATION AND DISCUSSION

To verify the validity of the proposed model, the prediction results are compared with those obtained by the 3-D FEA commercial package ANSOFT MAXWELL (ANSYS; Version No. 16.0; PA). The geometrical parameters and the physical properties used in the computations and further parametric analysis are listed in Table 1. For ease of comparison studies, the parameter values of PMs and conductor plate are derived from the similar research in [8] and [10]. The rate power of the case study is about 0.9 kW, thus the torque will be very small.

TABLE 1. Parameters of the studied model.

Symbol	Quantity	Value
l_1	Inner radius	30 mm
l_2	Outer radius	50 mm
h_1	Magnet weight	5 mm
p	Number of pole pairs	4
a (e-d)	Thickness of conductor disk	1 mm
b-a (d-c)	Air-gap length	1 mm
c-b	Thickness of iron core (magnet)	10 mm
h	Over length of conductor disk	10mm
q	Number of conductor par	16
σ	Conductivity of conductor	58 MS/m
B_r	Remanence of the PM	1.27 T
α (α_m)	Pole arc to pole pitch ratio	0.3
β_2	Spoke arc to slot pitch ratio	0.5
$K(k)$	Number of spatial harmonics used in region IIIi	19
$G(g)$	Number of spatial harmonics used in region Ii and Vi	15
$N(n)$	Number of spatial harmonics used in region II and IV	30
$M(m)$	number of time harmonics used in traveling magnetic field	7

It is worth noting that the sector magnets are difficult to magnetize, thus the rectangular magnets are employed and investigated in this case. According to the previous research [16], [18], the transformation of structure between the sector PM and the rectangular PM has to fulfill the following condition

$$\alpha_m < \frac{4p}{\pi}\frac{\alpha_r}{1+\alpha_r}\sin(\frac{\pi}{2p}) \quad \text{with} \quad \alpha_r = \frac{R_1}{R_2} \tag{63}$$

where, R_1 and R_2 are the inner and outer diameters, respectively; α_m is the ratio between the opening angle and the pole pith angle. In this paper, the following parameters are adopted: $R_1 = 30$ mm, $R_1 = 50$ mm, $\alpha_m = 0.3$. Therefore, the opening angle is $\beta = 0.3\pi/p$. In the FE model, the steel_1010 is employed, and its conductivity is 2×10^6 S/m.

Similar to the literatures available [1], [3], [10]–[12], there are mainly two constraints in the proposed analytical model. Before the further validation and discussion, we should know these constraints as follows

(1) The effects of the temperature factor on the material properties and torque characteristic has been neglected. However, the complex thermo-magnetic problems are solved in

our earlier study [30]. And in general, the toque value will drop with the increase of temperature.

(2) According to the assumptions, the 3-D effects on the field distribution have been neglected, thus only the flux density distributions at the mean radius are obtained and discussed. Although the flux density distributions along the radial direction have been discussed in some 2-D analytical models, the relationship between the flux density distributions and the radial coordinate is not made clear[24], [28]. And the complicated 3-D analytical model is the available method to solve this problem [19], [20].

A. FLUX DENSITY DISTRIBUTION

According to (49), (50), the flux density distributions in every domain can be predicted. Fig. 4 and Fig. 5 respectively show the axial and circumferential components of flux density distributions in the air gap region ($z = 1.5$ mm) at the low slip speed (40 r/min) and the high slip speed (400 r/min). In order to show the effectiveness and limitations of the analytical model, the analytical results will be compared with those obtained by 2-D FEM and 3-D FEM.

As indicated in Fig. 4 and Fig. 5, there are good agreements between the 2D analytical model and those obtained with 2-D FEM results. However, compared with the 3-D FEM results, there will be two alternatives: for the low slip speed values, they also have good agreements, but for the high speed values, there will be slight deviations between the proposed analytical model and the 3-D FEM. Many phenomena above indicate that the intentional neglect of induced currents flowing in the back iron and protrusions has little effect on the predictions, but the simplification of 3D geometrical structures will make influence on 2D analytical model in some degree, especially for the high slip speed values. Further investigations show that, with the increase of slip speed, the induced currents also increase, which exacerbates the inadaptability of the 2D analytical model. However, what is more noteworthy point is that the working area of such devices corresponds to the low slip values, because this is the high efficiency area [1], [2], and [27].

B. TORQUE AND AXIAL FORCE

Fig. 6 and Fig. 7 respectively show the comparison of torque prediction between 3D-FEM and analytical results at different values of air-gap length (1 mm and 3 mm). In order to present the influences of slotted conductor topology on torque characteristic, the eddy current coupling without slot in our previous research [10] is used as a comparison.

As indicated in Fig. 6 and Fig. 7, the analytical results are close to the 3-D FEM results. More detailed analysis for the torque curves is carried out, we can find that the deviation has changed with slip speed varying from 100 r/min to 1100 r/min. More specifically, for the low slip speed values, the discrepancies are minimal, but for the high slip speed values, the discrepancies are widen. Yet even so, the maximum deviation between these two methods is less than 15%. As previously described, with the increase of slip speed,

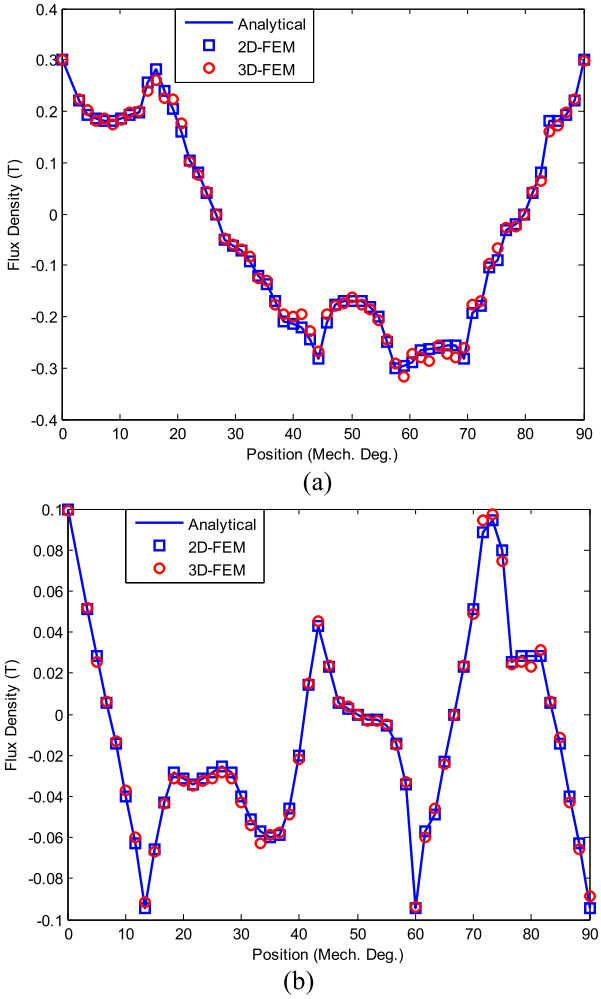

FIGURE 4. Flux density distribution in the air gap region ($z = 1.5$ mm) at a low slip speed ($n_1 s = 40$ r/min). (a) Axial component and (b) circumferential component.

the accuracy of the 2D analytical model will get worse, but the 3D correction factor (55) plays an important role in reducing the error. In fact, as discussion in [1] and [18], if only the R-N correction factor (54) is employed, the predicted results from the 2D analytical model will get worse. By comparing with the eddy current coupling without slotted conductor rotor, it can be found that the output torque of slotted topology is significantly improved, especially in the low slip speed region. When working in the high slip speed region, the advantage of slotted topology has gradually disappeared. One of the main reasons is that the eddy currents will be clustering in the conductor rotor for the high speed case, as shown in [18], therefore, the guide of eddy current based on slot is weakening. In addition, as shown in Fig. 6 and Fig. 7, with the increase of air-gap length, the output torque is rapidly decreasing, thus such devices are also widely used as the adjustable-speed drives [28].

Fig. 8 and Fig. 9 respectively show the variation of axial force for different values of air-gap length (1 mm and 3 mm). In order to better describe the force, the 2D analytical

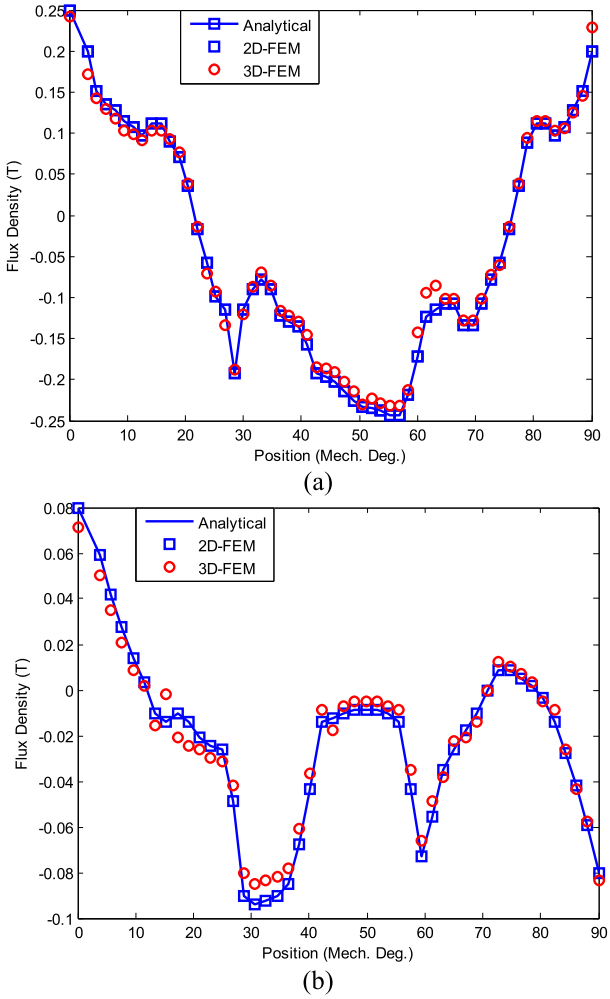

FIGURE 5. Flux density distribution in the air gap region ($z = 1.5$ mm) at a low slip speed ($n_1 s = 400$ r/min). (a) Axial component and (b) circumferential component.

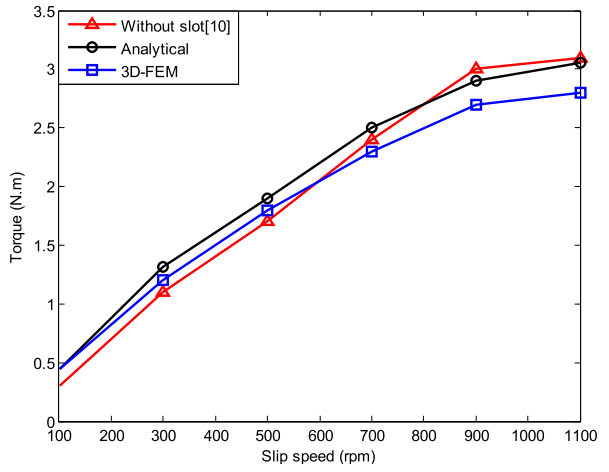

FIGURE 6. Comparison of torque characteristic obtained from analytical model, 3D-FEM, and the eddy current coupling having the same geometric parameters without slot topology [10] at the air gap length 1mm ($b - a$).

predictions are compared with the 3-D FEM results, and those obtained by [10]. As shown in Fig. 8 and Fig. 9, the axial force is well predicted by the analytical formula (62),

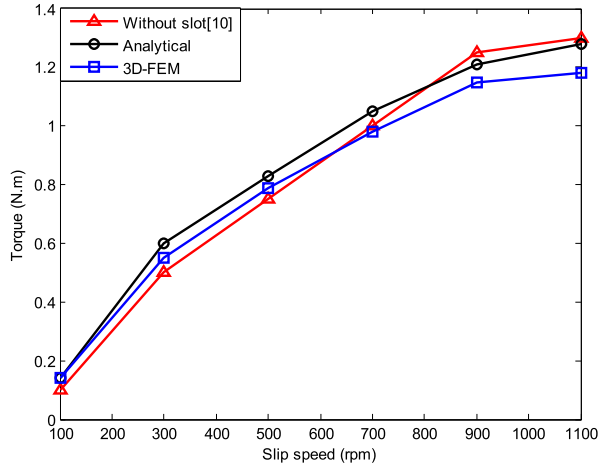

FIGURE 7. Comparison of torque characteristic obtained from analytical model, 3D-FEM, and the eddy current coupling having the same geometric parameters without slot topology [10] at the air gap length 3mm ($b - a$).

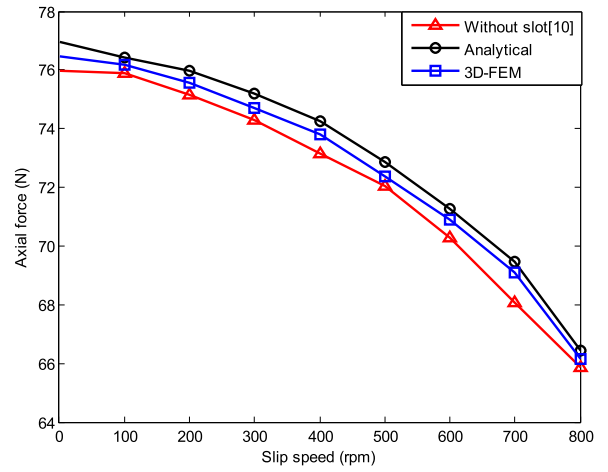

FIGURE 8. Comparison of axial force obtained from analytical model, 3D-FEM, and the eddy current coupling having the same geometric parameters without slot topology [10] at the air gap length 1mm ($b - a$).

and the maximum deviation between these two methods is less than 12%. Further analysis suggests the slight deviations mainly come from the 3D geometry effects. When the PM rotor and conductor rotor are relative stationary, the axial force is maximal, because the reaction field is null. Moreover, the axial force is mainly the attraction force. When the slip speed is increased, more induced currents are generated in the conductor disk, thus the stronger reaction field weakens the permanent magnetic field, which will lead to the decrease of the axial force. It is worth mentioning that when the slip speed exceeds a critical value, the axial force becomes the repulsive. In addition, we can observe that the axial forces from the slotted topology are larger than those from normal topology, because the air-gap magnetic flux density of the former are larger than the latter, especially in the low slip speed. Moreover, with the air gap length increasing, the axial force is sharply reduced.

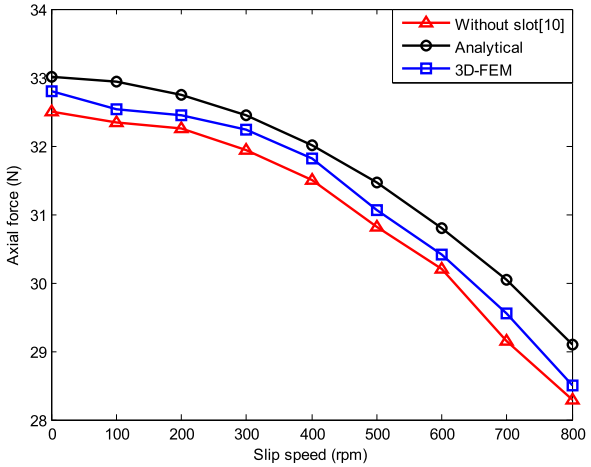

FIGURE 9. Comparison of axial force obtained from analytical model, 3D-FEM, and the eddy current coupling having the same geometric parameters without slot topology [10] at the air gap length 3mm ($b - a$).

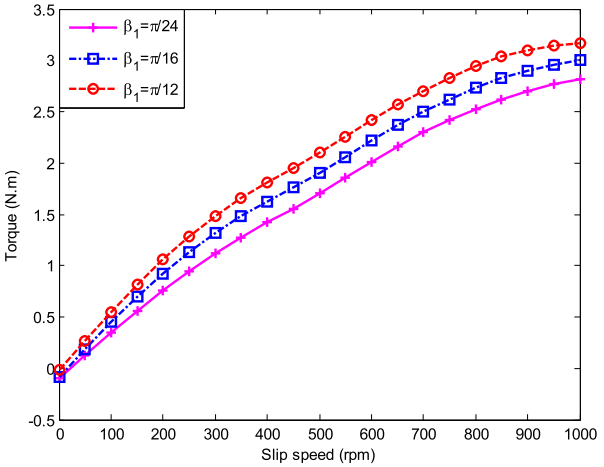

FIGURE 11. Torque characteristic comparison with different spoke angles (β_1), while $q = 16$.

C. INFLUENCE OF SLOT PARAMETERS ON TORQUE

For the eddy current coupling with slotted conductor rotor, the slot parameters have a great influence on the torque characteristics. Fig. 10 and Fig. 11 respectively present the variation of torque with the spoke number (q) and the spoke angle (β_1). As shown in Fig. 10 and Fig. 11, when the spoke number is increased from 8 to 24, while the spoke angle is kept constant ($\beta_1 = \pi/16$), the values of torque will enlarge accordingly; and when the spoke angle is increased from $\pi/24$ to $\pi/8$, while the spoke number is kept constant ($q = 16$), the values of torque will also enlarge. One of the interesting things is that these two approaches have changed the spoke arc to slot pitch ratio. Therefore, in a particular application, there will be a compromise between the spoke number and its angle. Taking into account the complexity of the manufacturing, the determination of spoke number and its angle will be converted into a rigorous optimization problem [11].

D. INFLUENCE OF PM PARAMETERS ON TORQUE

Fig. 12 and Fig. 13 respectively show the influences of the number of pole-pairs number (p), and the ratio between the inner diameter and outer diameter (α_r) on torque characteristics. As shown in Fig. 12, three values of α_r are discussed, respectively, $\alpha_r = 0.4$, $\alpha_r = 0.6$, and $\alpha_r = 0.8$, it is clear that there is a positive correlation between torque and α_r. In addition, at the fixed α_r, the torque will increase with the pole-pairs number, but with a decreasing tendency. As shown in Fig. 13, three values of pole-pairs number are investigated, respectively, $p = 4$, $p = 6$, and $p = 8$. Along with the increase of α_r, the torque values have the tendency of increasing first and then decreasing; for the parameters listed in Table 1, $\alpha_r = 0.65$ is the optimal value. However, as indicated in Fig. 13, according to different model parameters, α_r has different optimal value.

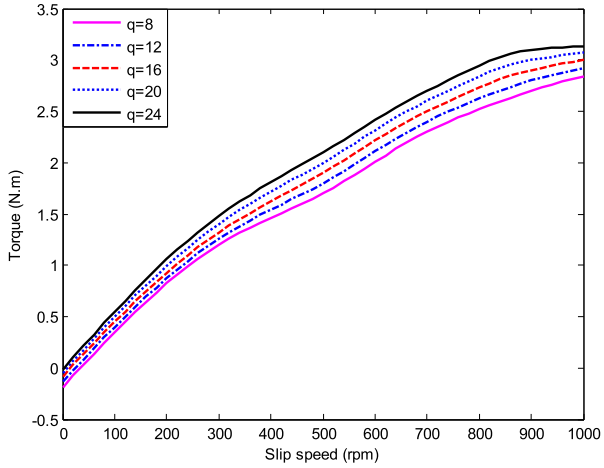

FIGURE 10. Torque characteristic comparison with different spoke numbers (q), while $\beta_1 = \pi/16$.

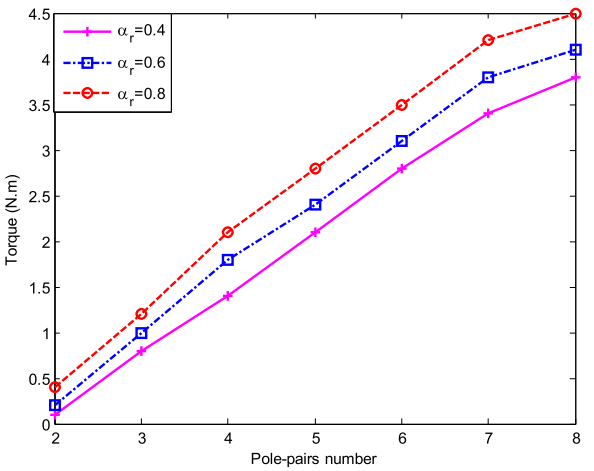

FIGURE 12. Variation of torque with pole-pairs number (p) and different α_r at a relative speed of 400 r/min.

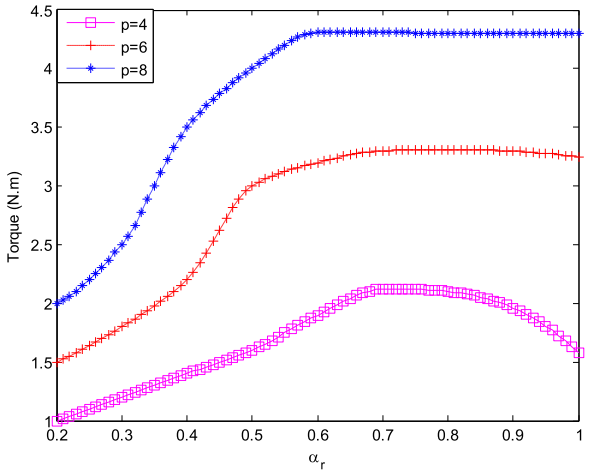

FIGURE 13. Variation of torque with α_r and different pole-pairs number (p) at a relative speed of 400 r/min.

E. SENSITICITY OF TORQUE ON HARMONIC PARAMETERS

The choice of harmonic parameters (K, M, G, and N) is a confusing problem. They are determined as a compromise between the accuracy and the computation time. In order to evaluate the sensitivity of analytic torque on K, M, G, and N, we will change one of the harmonic number, and leave the other parameters unchanged, as given in Table 1. Fig. 14 shows the variation of torque with each harmonic parameter.

As exhibited in Fig. 14, the torque values will be converged at different harmonic parameters, specifically, $N = 17$, $K = 13$, and $G = 7$. It also can be observed that the fundamental time harmonic component plays a dominant role in the computed torque. Although the number of harmonics is not fixed, they have the optimized values for each device's geometry. In addition, one area that may be of particular interest is that the computing time for 3-D FEM, employing a desktop PC (32 G (RAM) with 8 core), is about 300 min (20 points), while the computing time of the proposed analytical model is nearly all less than 3s. Therefore, the proposed 2-D analytical model can provide an effective approach in the parameter optimization process.

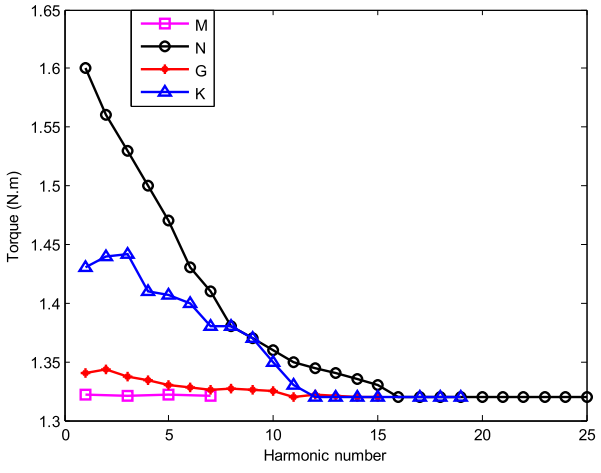

FIGURE 14. Sensitivity of the analytic torque on the number of harmonics (K, G, N, and M) at a relative speed of 300 r/min.

VI. CONCLUSION

In this paper, a flux-focusing eddy current coupling with double slotted conductor rotors is proposed. In order to evaluate its electromagnetic fields and forces, a two-dimensional analytical model is developed based on the accurate subdomain method. The slotting effects, as well as eddy currents effects in the conductor bars are considered in the analytical model.

By comparing with the 3-D FEM and 2-D FEM, it is found the flux density distribution obtained from the analytical model is in close agreement with 3-D FEM results, especially for the low slip speed (normal working area). Although three dimensional geometry is simplified, the expressions for the torque and axial force have sufficient accuracy. In addition, compared with the eddy current coupling without slotted conductor rotor, the topology in this paper has improved the torque performance.

Taking into account the computational time, the proposed analytical model provides an ideal alternative to the 3D FE simulations. Hence, it can be employed as a powerful tool for parametric analysis and design optimization of such devices.

APPENDIX

The complete forms of $\mathbf{M}$, $\mathbf{X}$, and $\mathbf{Y}$ in the linear equations (48) are given in (A.1), (A.2), and (A.3), as shown at the top of the next page, respectively. In (A.1), the subscript of element $M_*^{(1)} - M_*^{(50)}$ denotes the matrix dimensions (rows $\times$ columns); the subscript of element I_* denotes the dimension of the identity matrix; $(1)_*$ denotes the matrix with the element 1, whose subscript indicates the dimensions.

To simplify the analytical expressions, some notations are adopted as follows

$$E_{i,n} = \frac{\sin[n(\theta_i+\beta)] - \sin(n\theta_i)}{n} \tag{A.4}$$

$$F_{i,n} = \frac{\cos(n\theta_i) - \cos[n(\theta_i+\beta)]}{n} \tag{A.5}$$

$$\bar{E}_{i,n} = \frac{\sin[n(\alpha_i+\beta_1)] - \sin(n\alpha_i)}{n} \tag{A.6}$$

$$\bar{F}_{i,n} = \frac{\cos(n\alpha_i) - \cos[n(\alpha_i+\beta_1)]}{n} \tag{A.7}$$

$$P_{i,,n,k} = \frac{2}{\beta}\int_{\theta_i}^{\theta_i+\beta} \cos(n\theta)\cos[\lambda_k R_{av}(\theta-\theta_i)]d\theta \tag{A.8}$$

$$Q_{i,n,k} = \frac{2}{\beta}\int_{\theta_i}^{\theta_i+\beta} \sin(n\theta)\cos[\lambda_k R_{av}(\theta-\theta_i)]d\theta \tag{A.9}$$

$$\bar{P}_{i,n,g} = \frac{2}{\beta_1}\int_{\alpha_i}^{\alpha_i+\beta_1} \cos(n\theta)\cos[\lambda_g R_{av}(\theta-\alpha_i)]d\theta \tag{A.10}$$

$$\bar{Q}_{i,n,g} = \frac{2}{\beta_1}\int_{\alpha_i}^{\alpha_i+\beta_1} \sin(n\theta)\cos[\lambda_g R_{av}(\theta-\alpha_i)]d\theta \tag{A.11}$$

$$\mathbf{M}=\begin{bmatrix}
-I_q & 0 & (1)_{q\times 1} & M^{(1)}_{q\times N} & M^{(2)}_{q\times N} & M^{(3)}_{q\times N} & M^{(4)}_{q\times N} & 0 & 0 & 0\\
0 & -I_{qG} & 0 & M^{(5)}_{qG\times N} & M^{(6)}_{qG\times N} & M^{(7)}_{qG\times N} & M^{(8)}_{qG\times N} & 0 & 0 & 0\\
0 & 0 & 0 & -I_N & 0 & 0 & 0 & 0 & M^{(9)}_{N\times 2p} & M^{(10)}_{N\times 2pK}\\
M^{(12)}_{N\times q} & M^{(13)}_{N\times qG} & 0 & 0 & -I_N & 0 & 0 & 0 & 0 & 0\\
0 & 0 & 0 & 0 & 0 & -I_N & 0 & 0 & M^{(14)}_{N\times 2p} & M^{(15)}_{N\times 2pK}\\
M^{(17)}_{N\times q} & M^{(18)}_{N\times qG} & 0 & 0 & 0 & 0 & -I_N & 0 & 0 & 0\\
0 & 0 & (1)_{2p\times 1} & M^{(19)}_{2p\times N} & M^{(20)}_{2p\times N} & M^{(21)}_{2p\times N} & M^{(22)}_{2p\times N} & -I_{2p} & -bI_{2p} & 0\\
0 & 0 & 0 & 0 & 0 & 0 & 0 & -I_{2p} & -cI_{2p} & 0\\
0 & 0 & 0 & M^{(27)}_{2pK\times N} & M^{(28)}_{2pK\times N} & M^{(29)}_{2pK\times N} & M^{(30)}_{2pK\times N} & 0 & 0 & -I_{2pK}\\
0 & 0 & 0 & 0 & 0 & 0 & 0 & 0 & 0 & 0\\
0 & 0 & 0 & 0 & 0 & 0 & 0 & 0 & M^{(9)}_{N\times 2p} & M^{(35)}_{N\times 2pK}\\
0 & 0 & 0 & 0 & 0 & 0 & 0 & 0 & 0 & 0\\
0 & 0 & 0 & 0 & 0 & 0 & 0 & 0 & M^{(14)}_{N\times 2p} & M^{(39)}_{N\times 2pK}\\
0 & 0 & 0 & 0 & 0 & 0 & 0 & 0 & 0 & 0\\
0 & 0 & 0 & 0 & 0 & 0 & 0 & 0 & 0 & 0\\
0 & 0 & 0 & 0 & 0 & 0 & 0 & 0 & 0 & 0\\
(1)_{1\times q} & 0 & 0 & 0 & 0 & 0 & 0 & 0 & 0 & 0\\
0 & 0 & 0 & 0 & 0 & 0 & 0 & 0 & 0 & 0\\
0 & 0 & 0 & 0 & 0 & 0 & 0 & (1)_{1\times 2p} & 0 & 0
\end{bmatrix}$$

$$\begin{bmatrix}
0 & 0 & 0 & 0 & 0 & 0 & 0 & 0\\
0 & 0 & 0 & 0 & 0 & 0 & 0 & 0\\
M^{(11)}_{N\times 2pK} & 0 & 0 & 0 & 0 & 0 & 0 & 0\\
0 & 0 & 0 & 0 & 0 & 0 & 0 & 0\\
M^{(16)}_{N\times 2pK} & 0 & 0 & 0 & 0 & 0 & 0 & 0\\
0 & 0 & 0 & 0 & 0 & 0 & 0 & 0\\
0 & 0 & 0 & 0 & 0 & 0 & 0 & 0\\
0 & (1)_{2p\times 1} & M^{(23)}_{2p\times N} & M^{(24)}_{2p\times N} & M^{(25)}_{2p\times N} & M^{(26)}_{2p\times N} & 0 & 0\\
0 & 0 & 0 & 0 & 0 & 0 & 0 & 0\\
-I_{2pK} & 0 & M^{(31)}_{2pK\times N} & M^{(32)}_{2pK\times N} & M^{(33)}_{2pK\times N} & M^{(34)}_{2pK\times N} & 0 & 0\\
M^{(36)}_{N\times 2pK} & 0 & -I_N & 0 & 0 & 0 & 0 & 0\\
0 & 0 & 0 & -I_N & 0 & 0 & M^{(37)}_{N\times q} & M^{(38)}_{N\times qG}\\
M^{(40)}_{N\times 2pK} & 0 & 0 & 0 & -I_N & 0 & 0 & 0\\
0 & 0 & 0 & 0 & 0 & -I_N & M^{(41)}_{N\times q} & M^{(42)}_{N\times qG}\\
0 & (1)_{q\times 1} & M^{(43)}_{q\times N} & M^{(44)}_{q\times N} & M^{(45)}_{q\times N} & M^{(46)}_{q\times N} & -I_q & 0\\
0 & 0 & M^{(47)}_{qG\times N} & M^{(48)}_{qG\times N} & M^{(49)}_{qG\times N} & M^{(50)}_{qG\times N} & 0 & -I_{qG}\\
0 & 0 & 0 & 0 & 0 & 0 & 0 & 0\\
0 & 0 & 0 & 0 & 0 & 0 & (1)_{1\times q} & 0\\
0 & 0 & 0 & 0 & 0 & 0 & 0 & 0
\end{bmatrix} \tag{A.1}$$

$$\mathbf{X}=\begin{bmatrix}
\left(a_0^{Ii}\right)_q, \left(a_g^{Ii}\right)_{qG}, a_0^{II}, \left(a_n^{II}\right)_N, \left(b_n^{II}\right)_N, \left(c_n^{II}\right)_N, \left(d_n^{II}\right)_N, \left(a_0^{IIIi}\right)_{2p}, \left(b_0^{IIIi}\right)_{2p},\\
\left(a_k^{IIIi}\right)_{2pK}, \left(b_k^{IIIi}\right)_{2pK}, a_0^{IV}, \left(a_n^{IV}\right)_N, \left(b_n^{IV}\right)_N, \left(c_n^{IV}\right)_N, \left(d_n^{IV}\right)_N, \left(a_0^{Vi}\right)_q, \left(a_g^{Vi}\right)_{qG}
\end{bmatrix}^T \tag{A.2}$$

$$\mathbf{Y}=\left[0,0,\Gamma_N^{(1)},0,\Gamma_N^{(2)},0,0,0,0,0,\Gamma_N^{(1)},0,\Gamma_N^{(2)},0,0,0,0,0,0\right]^T \tag{A.3}$$

Then the matrices $M_*^{(1)} - M_*^{(50)}$ in (A.1) are expressed by

$$M_{q\times N}^{(1)} = \frac{1}{\lambda_n\beta_1 \mathrm{sh}[\lambda_n(b-a)]}\bar{E}_{i,n} \tag{A.12}$$

$$M_{q\times N}^{(2)} = \frac{\mathrm{cth}[\lambda_n(a-b)]}{\lambda_n\beta_1}\bar{E}_{i,n} \tag{A.13}$$

$$M_{q\times N}^{(3)} = \frac{1}{\lambda_n\beta_1 \mathrm{sh}[\lambda_n(b-a)]}\bar{F}_{i,n} \tag{A.14}$$

$$M_{q\times N}^{(4)} = \frac{\mathrm{cth}[\lambda_n(a-b)]}{\lambda_n\beta_1}\bar{F}_{i,n} \tag{A.15}$$

$$M_{qG\times N}^{(5)} = \frac{1}{\lambda_n \mathrm{sh}[\lambda_n(b-a)]}\bar{P}_{i,n,g} \tag{A.16}$$

$$M_{qG\times N}^{(6)} = \frac{\mathrm{cth}[\lambda_n(a-b)]}{\lambda_n}\bar{P}_{i,n,g} \tag{A.17}$$

$$M_{qG\times N}^{(7)} = \frac{1}{\lambda_n \mathrm{sh}[\lambda_n(b-a)]}\bar{Q}_{i,n,g} \tag{A.18}$$

$$M_{qG\times N}^{(8)} = \frac{\mathrm{cth}[\lambda_n(a-b)]}{\lambda_n}\bar{Q}_{i,n,g} \tag{A.19}$$

$$M_{N\times 2p}^{(9)} = \frac{1}{\pi}E_{i,n} \tag{A.20}$$

$$M_{N\times 2pK}^{(10)} = \frac{k\mathrm{cth}[\lambda_k(b-c)]}{2R_{av}}P_{i,,n,k} \tag{A.21}$$

$$M_{N\times 2pK}^{(11)} = \frac{k}{2R_{av}\mathrm{sh}[\lambda_k(c-b)]}P_{i,,n,k} \tag{A.22}$$

$$M_{N\times q}^{(12)} = \frac{1}{\pi}\Lambda_1\tanh(\Lambda_1 a)\bar{E}_{i,n} \tag{A.23}$$

$$M_{N\times qG}^{(13)} = \frac{\beta_1}{2\pi}\Lambda_2\tanh(\Lambda_2 a)\bar{P}_{i,n,g} \tag{A.24}$$

$$M_{N\times 2p}^{(14)} = \frac{1}{\pi}F_{i,n} \tag{A.25}$$

$$M_{N\times 2pK}^{(15)} = \frac{k}{2R_{av}\mathrm{sh}[\lambda_k(b-c)]}Q_{i,n,k} \tag{A.26}$$

$$M_{N\times 2pK}^{(16)} = \frac{k\mathrm{cth}[\lambda_k(c-b)]}{2R_{av}}Q_{i,n,k} \tag{A.27}$$

$$M_{N\times q}^{(17)} = \frac{1}{\pi}\Lambda_1\tanh(\Lambda_1 a)\bar{F}_{i,n} \tag{A.28}$$

$$M_{N\times qG}^{(18)} = \frac{\beta_1}{2\pi}\Lambda_2\tanh(\Lambda_2 a)\bar{Q}_{i,n,g} \tag{A.29}$$

$$M_{2p\times N}^{(19)} = \frac{\mathrm{cth}[\lambda_n(b-a)]}{\lambda_n\beta}E_{i,n} \tag{A.30}$$

$$M_{2p\times N}^{(20)} = \frac{1}{\lambda_n\beta \mathrm{sh}[\lambda_n(a-b)]}E_{i,n} \tag{A.31}$$

$$M_{2p\times N}^{(21)} = \frac{\mathrm{cth}[\lambda_n(b-a)]}{\lambda_n\beta}F_{i,n} \tag{A.32}$$

$$M_{2p\times N}^{(22)} = \frac{1}{\lambda_n\beta \mathrm{sh}[\lambda_n(a-b)]}F_{i,n} \tag{A.33}$$

$$M_{2p\times N}^{(23)} = \frac{\mathrm{cth}[\lambda_n(c-d)]}{\lambda_n\beta}E_{i,n} \tag{A.34}$$

$$M_{2p\times N}^{(24)} = \frac{1}{\lambda_n\beta \mathrm{sh}[\lambda_n(d-c)]}E_{i,n} \tag{A.35}$$

$$M_{2p\times N}^{(25)} = \frac{\mathrm{cth}[\lambda_n(c-d)]}{\lambda_n\beta}F_{i,n} \tag{A.36}$$

$$M_{2p\times N}^{(26)} = \frac{1}{\beta\lambda_n \mathrm{sh}[\lambda_n(d-c)]}F_{i,n} \tag{A.37}$$

$$M_{2pK\times N}^{(27)} = \frac{\mathrm{cth}[\lambda_n(b-a)]}{\lambda_n}P_{i,n,k} \tag{A.38}$$

$$M_{2pK\times N}^{(28)} = \frac{1}{\lambda_n \mathrm{sh}[\lambda_n(a-b)]}P_{i,n,k} \tag{A.39}$$

$$M_{2pK\times N}^{(29)} = \frac{\mathrm{cth}[\lambda_n(b-a)]}{\lambda_n}Q_{i,n,k} \tag{A.40}$$

$$M_{2pK\times N}^{(30)} = \frac{1}{\lambda_n \mathrm{sh}[\lambda_n(a-b)]}Q_{i,,n,k} \tag{A.41}$$

$$M_{2pK\times N}^{(31)} = \frac{\mathrm{cth}[\lambda_n(c-d)]}{\lambda_n}P_{i,n,k} \tag{A.42}$$

$$M_{2pK\times N}^{(32)} = \frac{1}{\lambda_n \mathrm{sh}[\lambda_n(d-c)]}P_{i,n,k} \tag{A.43}$$

$$M_{2pK\times N}^{(34)} = \frac{1}{\lambda_n \mathrm{sh}[\lambda_n(d-c)]}Q_{i,n,k} \tag{A.44}$$

$$M_{N\times 2pK}^{(35)} = \frac{k}{2R_{av}\mathrm{sh}[\lambda_k(b-c)]}P_{i,n,k} \tag{A.45}$$

$$M_{N\times 2pK}^{(36)} = \frac{k\mathrm{cth}[\lambda_k(c-b)]}{2R_{av}}P_{i,,n,k} \tag{A.46}$$

$$M_{2pK\times N}^{(33)} = \frac{\mathrm{cth}[\lambda_n(c-d)]}{\lambda_n}Q_{i,n,k} \tag{A.47}$$

$$M_{N\times q}^{(37)} = \frac{1}{\pi}\Lambda_1\tanh[\Lambda_1(d-e)]\bar{E}_{i,n} \tag{A.48}$$

$$M_{N\times qG}^{(38)} = \frac{\beta_1}{2\pi}\Lambda_2\tanh[\Lambda_2(d-e)]\bar{P}_{i,n,g} \tag{A.49}$$

$$M_{N\times 2pK}^{(39)} = \frac{k}{2R_{av}\mathrm{sh}[\lambda_k(b-c)]}Q_{i,,n,k} \tag{A.50}$$

$$M_{N\times 2pK}^{(40)} = \frac{k\mathrm{cth}[\lambda_k(c-b)]}{2R_{av}}Q_{i,,n,k} \tag{A.51}$$

$$M_{N\times q}^{(41)} = \frac{1}{\pi}\Lambda_1\tanh[\Lambda_1(d-e)]\bar{F}_{i,n} \tag{A.52}$$

$$M_{N\times qG}^{(42)} = \frac{\beta_1}{2\pi}\Lambda_2\tanh[\Lambda_2(d-e)]\bar{Q}_{i,n,g} \tag{A.53}$$

$$M_{q\times N}^{(43)} = \frac{1}{\lambda_n\beta_1 \mathrm{sh}[\lambda_n(c-d)]}\bar{E}_{i,n} \tag{A.54}$$

$$M_{q\times N}^{(44)} = \frac{\mathrm{cth}[\lambda_n(d-c)]}{\lambda_n\beta_1}\bar{E}_{i,n} \tag{A.55}$$

$$M_{q\times N}^{(45)} = \frac{1}{\lambda_n\beta_1 \mathrm{sh}[\lambda_n(c-d)]}\bar{F}_{i,n} \tag{A.56}$$

$$M_{q\times N}^{(46)} = \frac{\mathrm{cth}[\lambda_n(d-c)]}{\lambda_n\beta_1}\bar{F}_{i,n} \tag{A.57}$$

$$M_{qG\times N}^{(47)} = \frac{1}{\lambda_n \mathrm{sh}[\lambda_n(c-d)]}\bar{P}_{i,n,g} \tag{A.58}$$

$$M_{qG\times N}^{(48)} = \frac{\mathrm{cth}[\lambda_n(d-c)]}{\lambda_n}\bar{P}_{i,n,g} \tag{A.59}$$

$$M_{qG\times N}^{(49)} = \frac{1}{\lambda_n \mathrm{sh}[\lambda_n(c-d)]}\bar{Q}_{i,n,g} \tag{A.60}$$

$$M_{qG\times N}^{(50)} = \frac{\mathrm{cth}[\lambda_n(d-c)]}{\lambda_n}\bar{Q}_{i,n,g} \tag{A.61}$$

The elements of $\mathbf{X}$ in (A.2) are the column vectors, and the subscript indicates the dimension of each element. The elements of $\mathbf{Y}$ in (A.3) are also the column vector, mainly the zero vectors, and the special nonzero elements can be

expressed as

$$\Gamma_N^{(2)} = -\frac{1}{\pi}\sum_{i=1}^{2p}(-1)^i B_r F_{i,n} \tag{A.62}$$

$$\Gamma_N^{(1)} = -\frac{1}{\pi}\sum_{i=1}^{2p}(-1)^i B_r E_{i,n}. \tag{A.63}$$

REFERENCES

[1] T. Lubin and A. Rezzoug, "Steady-state and transient performance of axial-field eddy-current coupling," *IEEE Trans. Ind. Electron.*, vol. 62, no. 4, pp. 2287–2296, Apr. 2015.
[2] E. J. Davies, "An experimental and theoretical study of eddy-current couplings and brakes," *IEEE Trans. Power App. Syst.*, vol. 82, no. 67, pp. 401–419, Aug. 1963.
[3] A. Canova and B. Vusini, "Analytical modeling of rotating eddy-current couplers," *IEEE Trans. Magn.*, vol. 41, no. 1, pp. 24–35, Jan. 2005.
[4] A. S. Erasmus and M. J. Kamper, "Computationally efficient analysis of double PM-rotor radial-flux eddy current couplers," *IEEE Trans. Ind. Appl.*, vol. 53, no. 4, pp. 3519–3527, Apr. 2017.
[5] N. Amati, A. Tonoli, A. Canova, F. Cavalli, and M. Padovani, "Dynamic behavior of torsional eddy-current dampers: Sensitivity of the design parameters," *IEEE Trans. Magn.*, vol. 43, no. 7, pp. 3266–3277, Jul. 2007.
[6] Z. Mouton and M. J. Kamper, "Modeling and optimal design of an eddy current coupling for slip-synchronous permanent magnet wind generators," *IEEE Trans. Ind. Electron.*, vol. 61, no. 7, pp. 3367–3376, Jul. 2014.
[7] M. Enokizono *et al.*, "Development of high density and high efficiency machines," *J. Mater. Process. Technol.*, vol. 181, nos. 1–3, pp. 110–114, Jan. 2007.
[8] S. Mohammadi, M. Mirsalim, S. Vaez-Zadeh, and H. A. Talebi, "Analytical modeling and analysis of axial-flux interior permanent-magnet couplers," *IEEE Trans. Ind. Electron.*, vol. 61, no. 11, pp. 5940–5947, Nov. 2014.
[9] B. L. J. Gysen, E. Ilhan, K. J. Meessen, J. J. H. Paulides, and E. A. Lomonova, "Modeling of flux switching permanent magnet machines with fourier analysis," *IEEE Trans. Magn.*, vol. 46, no. 6, pp. 1499–1502, Jun. 2010.
[10] Z. Li, D. Wang, D. Zheng, and L. Yu, "Analytical modeling and analysis of magnetic field and torque for novel axial flux eddy current couplers with PM excitation," *AIP Adv.*, vol. 7, p. 105303, Oct. 2017.
[11] H. K. Razavi and M. U. Lampérth, "Eddy-current coupling with slotted conductor disk," *IEEE Trans. Magn.*, vol. 42, no. 3, pp. 405–410, Mar. 2006.
[12] Q. H. Liang, J. Mo, X. Dai, Y. Long, J. Cao, and S. Wang, "Modeling and analysis of field modulated permanent-magnet eddy-current couplings with a slotted conductor rotor," *Int. J. Appl. Electromagn. Mech.*, vol. 52, no. 3, pp. 1295–1303, Mar. 2016.
[13] H.-J. Shin, J.-Y. Choi, S.-M. Jang, and K.-Y. Lim, "Design and analysis of axial permanent magnet couplings based on 3D FEM," *IEEE Trans. Magn.*, vol. 49, no. 7, pp. 3985–3988, Jul. 2013.
[14] S. E. Gay and M. Ehsani, "Parametric analysis of eddy-current brake performance by 3-D finite-element analysis," *IEEE Trans. Magn.*, vol. 42, no. 2, pp. 319–328, Feb. 2006.
[15] M. H. Yas, M. Shakeri, M. Heshmati, and S. Mohammadi "Layer-wise finite element analysis of functionally graded cylindrical shell under dynamic load," *J. Mech. Sci. Technol.*, vol. 25, no. 3, pp. 597–604, Mar. 2011.
[16] L. Belguerras, L. Hadjout, S. Mezani, T. Lubin, and A. Rezzoug, "Study of HTS magnetic coupler using analytical and numerical computations," *IEEE Trans. Appl. Supercond.*, vol. 24, no. 6, pp. 1–12, Dec. 2014.
[17] A. Canova and B. Vusini, "Design of axial eddy-current couplers," *IEEE Trans. Ind. Appl.*, vol. 39, no. 3, pp. 725–733, May 2003.
[18] J. Wang, H. Lin, and S. Fang, "Analytical prediction of torque characteristics of eddy current couplings having a quasi-Halbach magnet structure," *IEEE Trans. Magn.*, vol. 52, no. 6, pp. 1–12, Jun. 2016.
[19] T. Lubin and A. Rezzoug "3-D analytical model for axial-flux eddy-current couplings and brakes under steady-state conditions," *IEEE Trans. Magn.*, vol. 51, no. 10, pp. 1–12, Apr. 2015.
[20] T. Lubin and A. Rezzoug "Improved 3-D analytical model for axial-flux eddy-current couplings with curvature effects," *IEEE Trans. Magn.*, vol. 53, no. 9, pp. 1–10, Sep. 2017.
[21] M.-C. Tsai, K.-Y. Chiou, S.-H. Wang, and C.-K. Lin, "Characteristics measurement of electric motors by contactless eddy-current magnetic coupler," *IEEE Trans. Magn.*, vol. 50, no. 11, Nov. 2014, Art. no. 8001209.
[22] A. Bellara, H. Bali, R. Belfkira, Y. Amara, and G. Barakat, "Analytical prediction of open-circuit eddy-current loss in series double excitation synchronous machines," *IEEE Trans. Magn.*, vol. 47, no. 9, pp. 2261–2268, Sep. 2011.
[23] Z. Q. Zhu, L. J. Wu, and Z. P. Xia "An accurate subdomain model for magnetic field computation in slotted surface-mounted permanent-magnet machines," *IEEE Trans. Magn.*, vol. 46, no. 4, pp. 1100–1115, Apr. 2010.
[24] T. Lubin, S. Mezani, and A. Rezzoug "Development of a 2-D analytical model for the electromagnetic computation of axial-field magnetic gears," *IEEE Trans. Magn.*, vol. 49, no. 11, pp. 5507–5521, Nov. 2013.
[25] J. Wang, H. Lin, S. Fang, and Y. Huang "A general analytical model of permanent magnet eddy current couplings," *IEEE Trans. Magn.*, vol. 50, no. 1, Jan. 2014, Art. no. 8000109.
[26] J. H. Wouterse, "Critical torque and speed of eddy current brake with widely separated soft iron poles," *IEE Proc. B Electr. Power Appl.*, vol. 138, no. 4, pp. 153–158, Jul. 1991.
[27] S. Mohammadi, M. Mirsalim, and S. Vaez-Zadeh "Nonlinear modeling of eddy-current couplers," *IEEE Trans. Energy Convers.*, vol. 29, no. 1, pp. 224–231, Mar. 2014.
[28] X. Dai, J. Cao, Y. Long, Q. Liang, J. Mo, and S. Wang, "Analytical modeling of an eddy-current adjustable-speed coupling system with a three-segment Halbach magnet array," *Electr. Power Compon. Syst.*, vol. 43, no. 17, pp. 1891–1901, Sep. 2015.
[29] X. Dai, Q. Liang, J. Cao, Y. Long, J. Mo, and S. Wang, "Analytical modeling of axial-flux permanent magnet eddy current couplings with a slotted conductor topology," *IEEE Trans. Magn.*, vol. 52, no. 2, Feb. 2016, Art. no. 8000315.
[30] D. Zheng, D. Wang, S. Li, T. Shi, Z. Li, and L. Yu "Eddy current loss calculation and thermal analysis of axial-flux permanent magnet couplers," *AIP Adv.*, vol. 7, p. 025117, Feb. 2017.

ZHAO LI received the B.S. degree in electrical engineering from the Henan University of Science and Technology, Luoyang, China, in 2009, and the M.S. degree in control theory and control engineering from Northeastern University, Shenyang, China, in 2012, where he is currently pursuing the Ph.D. degree.

He became an Engineer with Xuji Group Corporation from 2012 to 2014. His current research interests include the analysis and design of electromagnetic systems, and motion control.

DAZHI WANG received the M.S. degree in control theory and control engineering from the Shenyang University of Technology, Shenyang, China, in 1992, and the Ph.D. degree in control theory and control engineering from Northeastern University, Shenyang, China, in 2003.

From 1992 to 1994, he was a Post-Doctoral Fellow with the Shenyang University of Technology, Shenyang, China. From 1992 to 1993, he also did Post-Doctoral Research with Hochschule Aalen, Aalen, Germany. Since 2003, he has been with Northeastern University, where he is currently a Full Professor with the School of Information Science and Engineering. He is also the Director of the Institute of Electric Power System and Power Transmission and the Northeastern University-Schneider Electric (France) Laboratory, Northeastern University, Shenyang. He has authored over 40 technical papers and holder of 10 patents. His main research is related to the design, analysis, and control of permanent magnet motors, intelligent electrical apparatus, and power system.

DI ZHENG was born in Heilongjiang, China. She received the B.Eng. and M.Eng. degrees in electrical engineering from Northeastern University, Shenyang, China, in 2012 and 2015, respectively, where she is currently pursuing the Ph.D. degree in power electronics and power transmission. Her current research interests include design and analyze permanent magnet couplers in magnetic field and thermal field.